

M. Akgul, A. Ozgurluk, and C. T.-C. Nguyen, "RF channel-select micromechanical disk filters—part II: demonstration," *IEEE Trans. Ultrason., Ferroelect., Freq. Contr.*, vol. 66, no. 1, pp.218-235, Jan. 2019, DOI: [10.1109/TUFFC.2018.2883296](https://doi.org/10.1109/TUFFC.2018.2883296). (18 pages).

RF Channel-Select Micromechanical Disk Filters, Part II: Demonstration

Mehmet Akgul, *Member, IEEE*, Alper Ozgurluk, *Student Member, IEEE*, and Clark T.-C. Nguyen, *Fellow, IEEE*

Abstract—This part II of a two-paper sequence presents fabrication and measurement results for a micromechanical disk-based RF channel-select filter designed using the theory and procedure of Part I. Successful demonstration of an actual filter required several practical additions to an ideal design, including the introduction of a 39nm-gap capacitive transducer, voltage-controlled frequency tuning electrodes, and a stress relieving coupled array design, all of which combine to enable a 0.1%-bandwidth 223.4-MHz channel-select filter with only 2.7dB of in-band insertion loss and 50dB rejection of out-of-band interferers. This amount of rejection is more than 23dB better than a previous capacitive-gap transduced filter design that did not benefit from sub-50nm gaps. It also comes in tandem with a 20dB shape factor of 2.7 realized by a hierarchical mechanical circuit design utilizing 206 micromechanical circuit elements, all contained in an area footprint of only 600 $\mu\text{m}\times$ 420 μm . The key to such low insertion loss for this tiny percent bandwidth is Q 's $>8,800$ supplied by polysilicon disk resonators employing for the first time capacitive transducer gaps small enough to generate coupling strengths of $C_x/C_o \sim 0.1\%$, which is a 6.1 \times improvement over previous efforts. The filter structure utilizes electrical tuning to correct frequency mismatches due to process variations, where a dc tuning voltage of 12.1V improves the filter insertion loss by 1.8dB and yields the desired equiripple pass-band shape. Measured filter performance, both in- and out-of-channel, compare well with predictions of an electrical equivalent circuit that captures not only the ideal filter response, but also parasitic non-idealities that distort somewhat the filter response.

Index Terms—RF channel selection, MEMS resonator, band-pass filter, insertion loss, spurious mode, stress control, feed-through, coupling, small gap, frequency tuning, microfabrication.

I. INTRODUCTION

Having presented a complete design procedure for filters utilizing capacitive-gap transduced micromechanical disk resonators in Part I of this two-part paper, Part II now turns to practical implementation issues. In particular, unlike the ideal filter covered in Part I, a real filter suffers non-idealities that if not circumvented can significantly compromise performance. Among the most important practical considerations for the present design are:

- 1) Structural film stress, especially in-plane stress that might push resonators into their substrate-anchored electrodes.
- 2) Parasitic trace resistance that might contribute significant insertion loss and increase input to output feedthrough.
- 3) Finite fabrication tolerances that introduce frequency variations, most importantly frequency mismatches between

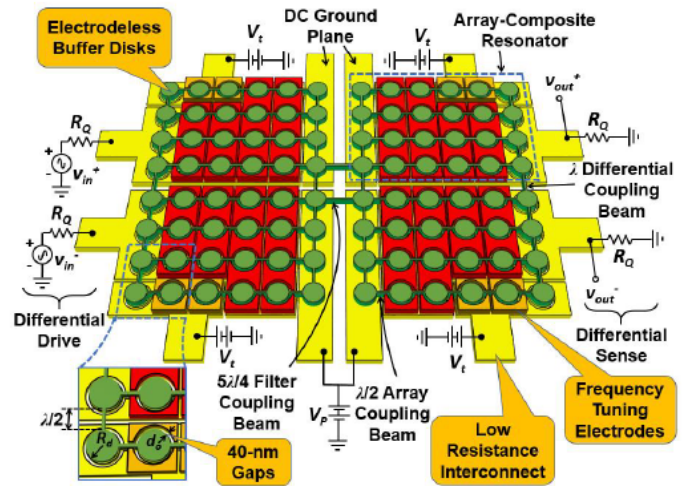


Fig. 1: Schematic description of the demonstrated 2nd order differential filter, showing the electrical drive and sense measurement setup and emphasizing key features that make possible practical implementation of this mechanical circuit.

identically designed resonators.

Pursuant to elucidating, understanding, and alleviating the impact of these and other non-idealities, this Part II paper demonstrates an actual polysilicon surface-micromachined filter designed using the methods of Part I. The demonstrated 223.4-MHz second order Chebyshev filter, *cf.* Fig. 1, employs 206 resonant micromechanical elements to realize a channel-selecting 0.1%-bandwidth while achieving only 2.7dB of in-band insertion loss together with 50dB of out-of-channel stop-band rejection [1]. This amount of rejection is 23dB better than that of previous capacitive-gap transduced channel-select filter efforts [2], and comes in tandem with a 20dB shape factor of 2.7 commensurate with its use of two array-composite resonators. Capacitive transducer gaps scaled down to 39nm and a bias voltage of 14V achieve sufficient single-resonator transducer coupling strengths of $C_x/C_o = 0.1\%$ and a low filter termination impedance of only 590 Ω . As shown in Fig. 1, the filter comprises 96 disks mechanically coupled by 110 beams. The clearly discernable mechanically coupled resonator arrays implement a design hierarchy reminiscent of complex VLSI transistor circuits, but here used to achieve a complex MSI mechanical filter circuit [3].

The paper begins by addressing each of the three practical considerations enumerated above and describing defensive design solutions. These include electrodeless buffer devices that

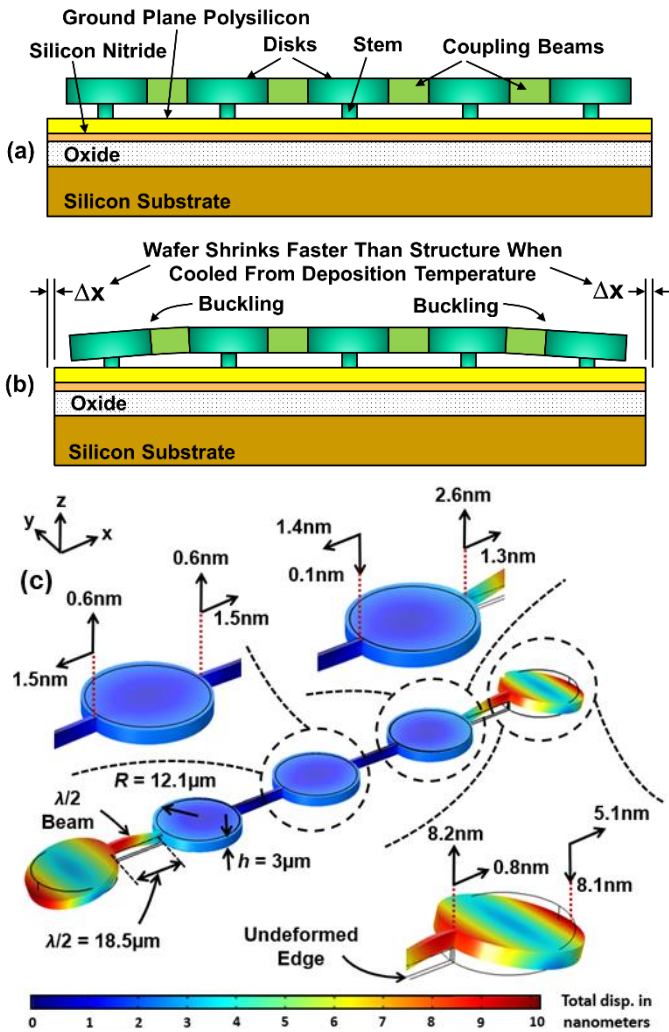


Fig. 2: (a) Cross-section of a linear disk array-composite under no stress. (b) The same cross-section but now with stress induced by faster thermal contraction of the substrate relative to the structure as the temperature falls from deposition to room temperature, where stem anchors moving with the structure exert stress on the array-composite structure. (c) Finite element stationary analysis result for a 1×5 polysilicon disk resonator array-composite under 50 MPa compressive stress. Each disk is substrate-anchored at the center by a stem post $2\mu\text{m}$ in diameter and connected to the adjacent disk by $\lambda/2$ -long beams. The color-map legend indicates displacement in nanometers. The x - and z -directed arrows in the zoom-ins indicate lateral and vertical displacements.

alleviate post-fabrication stress to prevent undue disk-to-electrode contact in Section II; thick conductive interconnect layers that greatly reduce parasitic resistance, thereby reducing insertion loss and increasing isolation, in Sections III and IV; and non-input/output (I/O) devices specifically tasked to provide voltage-controlled electrical stiffness frequency tuning to compensate for finite fabrication tolerances in Section V. After summarizing the demonstrated filter design in Section VI, the paper proceeds to describe the fabrication process flow in Section VII, then present measurements that match well to theoretical predictions in Section VIII.

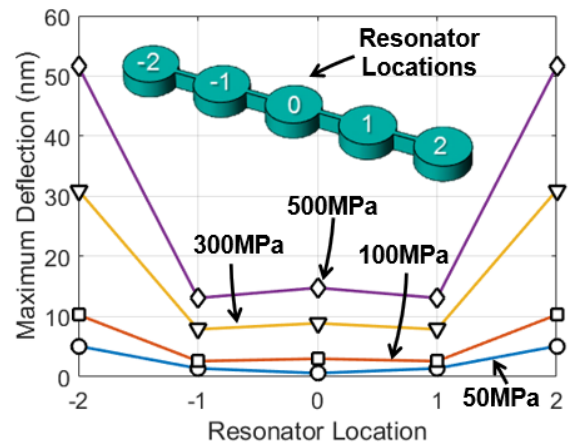


Fig. 3: Plot of FEA static analysis results for maximum static displacement under four different structural film stress scenarios for the structure of Fig. 2.

II. DEFENSIVE DESIGN AGAINST FILM STRESS

Part I of this study emphasized the importance of small electrode-to-resonator gaps that amplify the input/output electromechanical coupling and directly contribute to large stop-band rejection. Indeed, small gaps have greatly enhanced the electromechanical coupling coefficients of the single disks of [4] and [5].

Unfortunately, going from a single resonator to an ensemble of mechanically linked ones introduces a yield loss mechanism that intensifies as gaps become smaller. In particular, differences in substrate and structural material thermal expansion coefficients generate strains when the temperature drops from the structural material deposition temperature to room temperature that effectively move certain resonators in the network relative to their electrodes. If strains are large enough, resonators can actually push into their electrodes, shorting the two in a way that would debilitate the whole filter. Clearly, the problem becomes worse as electrode-to-resonator gap spacing shrinks.

Fig. 2 illustrates the problem for the case of a linear array of five identical 224-MHz polysilicon contour mode disk resonators, each $3\mu\text{m}$ -thick with $12.1\mu\text{m}$ -radius, all coupled via half-wavelength extensional-mode beams. $2\mu\text{m}$ -diameter center stem anchors suspend each disk $0.5\mu\text{m}$ above the substrate. Here, a stationary finite element analysis (FEA) reveals that the strain in a string of half-wavelength coupled disks under the typical (for polysilicon over silicon) 50 MPa of in-plane compressive stress translates to the end disks, leaving the inner disks relatively strain free. For the specific case of Fig. 2, the outer edges of the end disks move 5.1 nm along the string axis, which is $2\times$ larger than the maximum 2.6 nm experienced by the inner disks. This is fortuitous, indeed, and suggests that gap-closing strains alleviate by merely employing electrodeless buffer disks at the ends of any string of coupled disks that absorb most of the strain, allowing the inner disks to sport electrodes spaced very close to them with reasonable resilience against stress.

To further quantify the permissible set of array lengths as a function of residual stress, Fig. 3 plots the maximum displacement experienced by each disk in the Fig. 2 5-disk linear array under four different residual stress conditions, with some much larger than normal. The plot more clearly illustrates how the

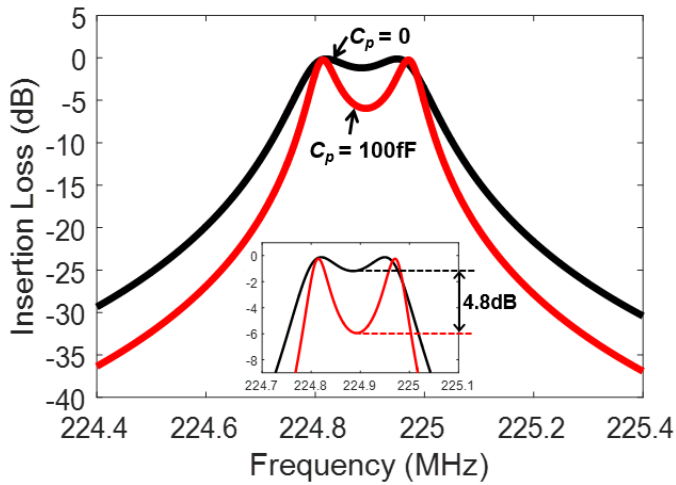


Fig. 4: Simulated frequency response spectra for a 225-MHz two-pole, i.e. two-resonator, 0.5dB-ripple, Chebyshev filter with 0.1% bandwidth, for small and large values of pad capacitance.

inner disks experience very similar displacements that gradually increase with stress, while displacements at the end disk increase much more abruptly with increasing stress. An important takeaway from Fig. 3 is that a 5-disk linear array (such as used in the demonstrated filter) cannot safely support 40nm electrode-to-disk gaps if post fabrication residual stress values rise above 1.5GPa. Fortunately, well-designed deposition recipes provide stress levels below 200 MPa for the majority of useful micromachinable materials, where 50 MPa is typical for properly annealed polysilicon.

Interestingly, according to FEA simulation, the use of just two buffer devices as in Fig. 3 is just as effective for much larger arrays, as well. For example, a 9-disk array with two buffer devices incurs less than 1-nm increase in inner disk movement over a 5-disk one.

The area penalty incurred when employing stress-relieving electrodeless buffer disks at the boundaries of each of the four arrays is clear from Fig. 1, where the penalty amounts to a 50% increase in disk footprint over the electroded 4×4 array. The penalty for doing this manifests in not only area, but also electromechanical coupling, which reduces from the 0.128% it would have been without the buffer disks, to 0.074% with the buffer disks, as predicted by (40) from Part I for the filter design presented in Table I (later). As will be seen in Section VIII, these encumbrances are well worth the yield enhancement afforded via these buffer disks.

III. IMPACT OF PARASITICS

As with any micro-scale on-chip device, parasitic resistance and capacitance can impact the performance of a micromechanical filter, and their influence increases as frequency increases. Of the two, resistance is perhaps the most controllable, which is fortunate, since resistance can often serve as an effective knob with which to control capacitive parasitics.

The capacitive parasitics that most impact filter performance are shunt capacitance at the input and output terminals; and feedthrough capacitors that offer an alternative signal path for input signals thereby competing with the filter path.

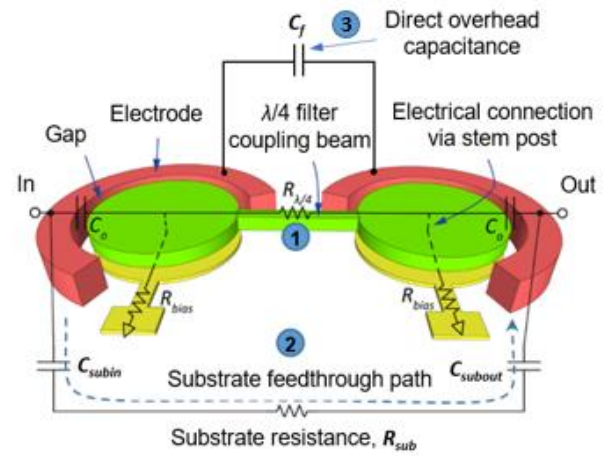


Fig. 5: Schematic description of dominant electrical feedthrough paths in a simple two-resonator filter.

A. Shunt Parasitic Capacitance

Part I described the importance of electromechanical coupling (C_x/C_o) to avoid passband distortion, where (C_x/C_o) should be greater than the intended percent bandwidth by a factor governed by the filter order, which in turn depends upon the number of resonators used. Note that (39) from Part I for (C_x/C_o) accounts for only the intrinsic electrode-to-resonator overlap C_o and not any parasitic capacitance. If additional capacitance C_p from parasitic sources adds to the intrinsic value, the value of (C_x/C_o) changes by the factor

$$\left(\frac{C_x}{C_o}\right)_{eff} = \frac{1}{1 + C_p/C_o} \left(\frac{C_x}{C_o}\right) \quad (1)$$

which could entail a significant reduction if C_o is small compared with C_p . For example, the 12.1 μ m-radius disks used in the prototype of this work have shunt C_o 's of 47.4fF. If a single resonator were used as an input device, biased as in Table I, then an 80 μ m × 80 μ m bond pad that alone adds 97.7fF of shunt capacitance through the 500nm nitride and 2 μ m oxide layers would reduce (C_x/C_o) by 3×, from 0.1% to 0.034%. Fig. 4 illustrates via simulation the 4.8dB of additional passband distortion imposed by this bond pad capacitance. This much distortion is generally not acceptable.

One method to obviate shunt capacitance, whether parasitic or intrinsic, is to resonate it out via an inductor. The obvious issue here is the need for an inductor, which whether on or off chip, incurs undesirable cost increase. Still, this solution makes good sense if that one inductor can resonate the shunt capacitance of many filters all at once, such as would be possible for an RF channel-selecting bank of filters [6]. If only one filter, however, the use of an inductor to resonate out shunt capacitance is not cost effective.

Equation (1) suggests that an alternative solution that avoids the need for an inductor is simply to increase the intrinsic C_o of the resonator relative to C_p . Indeed, once C_o dominates over C_p , the parasitic has much less influence. Perhaps the most effective way to do this is to decrease the electrode-to-resonator gap spacing, since this raises C_x faster than C_o , raising the overall (C_x/C_o) while increasing immunity against C_p .

If reducing gap spacing is not an option, however, then the next best solution is as shown in Fig. 1, where the use of disk

array-composites increases the intrinsic C_o and the C_x at the same rate, keeping (C_x/C_o) constant, while attenuating the effect of C_p via (1). In the specific prototype demonstrated here, ignoring for now the effect of buffer disks, the use of 16 I/O disks in each quadrant array generates 800fF of intrinsic C_o , which now limits the reduction in (C_x/C_o) to only 1.1 \times , yielding a $(C_x/C_o)_{eff}$ of 0.089%.

Finally, another reasonable strategy to reduce C_p is to float the substrate, which would work best if the substrate were non-conductive. The prototype filter demonstrated here actually takes this approach, i.e., does not ground the substrate. However, its substrate is not un-doped, but rather lightly-doped with a resistivity of 8-12 Ω -cm. Although this does reduce shunt capacitance, it also introduces additional feedthrough, which can both distort the passband and reduce the stopband rejection. Use of a high resistance substrate would likely have fared better. Obviously, this approach all but precludes integration over bulk CMOS. If integration over CMOS were available and desired, though, other approaches to suppressing shunt capacitance arise in tandem, such as ground plane bootstrapping.

B. Feedthrough Parasitics

Fig. 5 depicts the parasitic resistors and capacitors that most impact the performance of a simple two-resonator filter. These include:

- 1) the physical resistors R_{bias} from the actual dc-bias voltage supply to the disk-to-electrode interfaces;
- 2) the resistance $R_{\lambda/4}$ between the disks, mainly through the coupling beam;
- 3) the electrode-to-resonator overlap capacitors, C_o ; and
- 4) the feedthrough path from input electrode to output electrode, which comprises the series combination of substrate capacitors C_{sub} 's, plus series resistance, as well as direct overhead capacitance C_f between the electrodes.

Of particular concern are parasitic elements that permit electrical feedthrough of signals from input to output that effectively bypass the filter transfer function. Here, electrical feedthrough can generate significant passband distortion and reduce out-of-band rejection, thereby compromising the filter's ability to eliminate out-of-channel blockers.

Of the paths available for feedthrough in Fig. 5, three stand out as most troublesome:

- 1) *Through-Structure Feedthrough (Path 1)* starting at the input electrode, going through the input electrode-to-disk capacitor, through the structure resistance (dominated by the coupling beam's $R_{\lambda/4}$), and finally through the disk-to-output electrode overlap capacitor to the output electrode.
- 2) *Through-Substrate External Feedthrough (Path 2)* going through the input electrode-to-substrate capacitor, through the substrate resistance, and finally out the substrate-to-output electrode capacitor to the output electrode. Note that in a practical research design that allows interrogation via probe, or in a situation where MEMS and other function dies connect via wire-bonds, bond pads can greatly increase the electrode-to-substrate capacitance.
- 3) *Overhead External Feedthrough (Path 3)* going from input to output through direct parasitic feedthrough capacitance, perhaps going over the structure itself. This component can

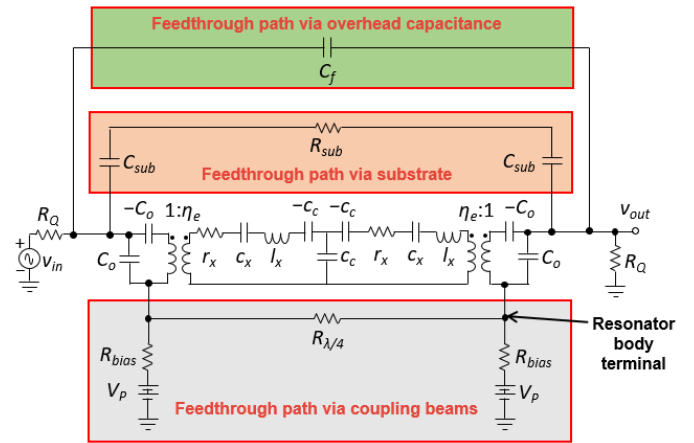


Fig. 6: Circuits for the parasitic paths Fig. 5 hooked around the circuit for a properly terminated two-resonator filter with input source v_{in} and output v_{out} .

be particularly important in situations where probe station probe tips or bond wires access the filter.

Insight on methods to suppress these feedthrough paths follows most readily from inspection and simulation of the equivalent circuit modeling the filter and its parasitic elements.

IV. FILTER ELECTRICAL EQUIVALENT CIRCUIT WITH PARASITIC ELEMENTS

Of course, the entire filter is more complex than the simple two-resonator illustration of Fig. 5, as it contains arrays of disks and a fully differential structure. Unfortunately, complexity like this can hide significant insight. In the interest of gleaning maximum insight, it is instructive to tackle first the much simpler equivalent circuit of the Fig. 5 two-resonator filter.

A. Case: Single-Ended Filter

Pursuant to this, Fig. 6 inserts the simple parasitic path circuit of Fig. 5 into a properly terminated drive and sense circuit with input source v_{in} and output v_{out} . From this circuit, depending on the values of internal parasitic resistors R_{bias} and $R_{\lambda/4}$, the amount of source signal v_{in} traversing the feedthrough path and appearing at the output becomes a strong function of the value of R_Q .

i. Suppressing Series External Feedthrough (Paths 2 and 3)

Simple inspection of the Fig. 6 circuit reveals that the purely series feedthrough paths, i.e., paths 2 and 3, experience greater attenuation with smaller values of R_Q . In particular, the transfer function for the overhead feedthrough path from v_{in} to v_{out} takes the form

$$\frac{v_{out}}{v_{in}} = \frac{j\omega R_Q C_f}{1 + j2\omega R_Q C_f} \quad (2)$$

Here, reducing R_Q from 5k Ω to 50 Ω would decrease the feedthrough level by 39.9dB at 223MHz for a C_f value of 10fF.

For the through substrate feedthrough path, the expression relating the voltage seen at v_{out} to that at v_{in} takes the form

$$\frac{v_{out}}{v_{in}} = \frac{j\omega R_Q C_{sub}}{2 + j\omega(2R_Q + R_{sub})C_{sub}} \quad (3)$$

Again, a need to reduce R_Q manifests, where reducing R_Q from $5\text{k}\Omega$ to 50Ω would decrease the feedthrough level by 33.12dB at 223MHz for typical C_{sub} and R_{sub} values of 530.5fF and 374.98Ω , respectively.

Beyond this, consideration of the external feedthrough path 2 suggests that the magnitude of unwanted current in an asymmetric structure is best suppressed by shrinking bond pads and increasing the isolation dielectric layer thickness (*cf.* Fig. 13) to reduce capacitance from the I/O ports to the substrate; and by raising the substrate resistance, perhaps by using an undoped silicon substrate.

ii. Suppressing Through-Structure Feedthrough (Path 1)

In Fig. 6 signals feeding through the structure itself first proceed through the input capacitance, then through a resistive voltage divider comprised of the R_Q , R_{bias} , and $R_{\lambda/4}$ resistors. The element values of the resistors in this voltage divider largely determine how much signal shunts to ac ground (realized by dc-bias sources) and how much makes it to the output. Assuming R_Q is much larger than R_{bias} and $R_{\lambda/4}$, the expression relating the voltage seen at v_{out} to that at v_{in} is

$$\frac{v_{out}}{v_{in}} \approx \left\{ \frac{j\omega R_{bias} C_o}{1 + j\omega R_Q C_o} \frac{1 + \frac{R_{\lambda/4}}{R_{bias}}}{2 + \frac{R_{\lambda/4}}{R_{bias}}} \right\} \left\{ \frac{1}{1 + \frac{R_{\lambda/4}}{R_{bias}}} \right\} \left\{ \frac{j\omega R_Q C_o}{1 + j\omega R_Q C_o} \right\} \quad (4)$$

Equation (4) reveals that for cases where through-structure feedthrough dominates over external paths, there is a worst-case value of R_Q where the equation (4) transfer function peaks (which of course is bad). Fig. 7 plots (4) at 223MHz versus the value of R_Q for typical values of structural parasitic elements: $R_{bias} = 5.85\Omega$, $R_{\lambda/4} = 10\Omega$, and $C_o = 648\text{fF}$. Here, the worst-case value of R_Q is $1,101\Omega$, at which the feedthrough level peaks to -62.9dB at 223MHz . From the plot, when through-structure feedthrough dominates over other paths, it is best to pick either small or large values of R_Q . This is fortuitous given that most practical IF and RF applications prefer impedances on the smaller side, in the 50Ω to 500Ω range.

Equation (4) further suggests that feedthrough plummets when interconnect resistance, e.g. R_{bias} , is minimized while structure resistance, e.g., $R_{\lambda/4}$, is maximized. As shown in Fig. 8(b), the R_{bias} resistors associated with dc-bias interconnects effectively shunt to ground currents that would otherwise feedthrough to the output. The smaller the value of R_{bias} , the larger the amount of current that takes the path towards the dc-bias pads, and the less parasitic current that reaches the output. In contrast, a high R_{bias} resistance between the dc-bias source and the disk resonator effectively repels current, directing it towards the output port instead of the dc-bias sink, *cf.* Fig. 8(c), where it can mask the desired motional current of the device and limit the ultimate filter stopband rejection. This justifies the added fabrication process complexity to achieve $3\mu\text{m}$ -thick phosphorus doped polysilicon interconnect traces in this study, which are considerably thicker than the 300nm of previous work [2], so much more conductive. The $3\mu\text{m}$ -thick interconnect of this work provides a sheet resistance on the order of $0.8\Omega/\square$, which is considerably smaller than the $21.3\Omega/\square$ of previous 300nm -thick traces. As will be seen, this greatly improves the stopband rejection of the demonstrated filter.

Low parasitic trace resistance not only minimizes parasitic

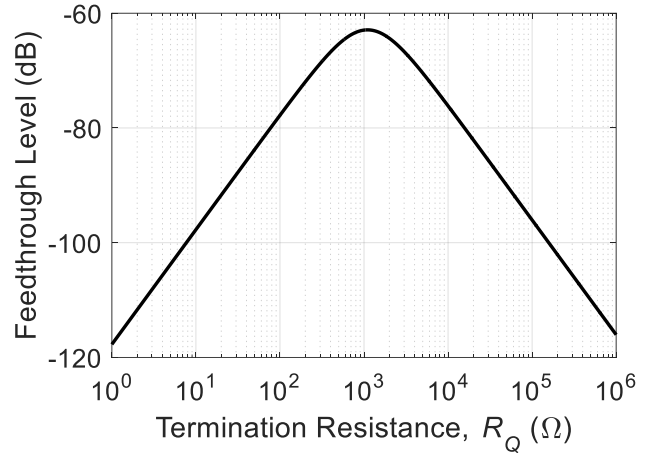


Fig. 7: Through structure feedthrough at 223MHz versus the value of R_Q for typical values of structural parasitic elements: $R_{bias} = 5.85\Omega$, $R_{\lambda/4} = 10\Omega$, and $C_o = 648\text{fF}$.

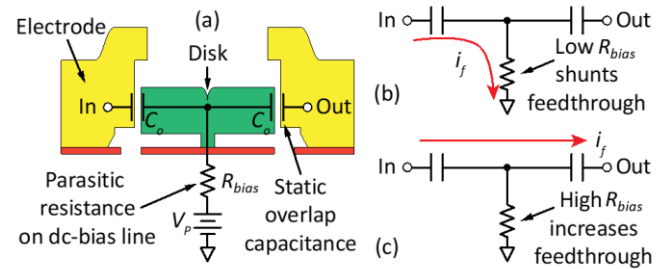


Fig. 8: (a) Schematic describing the current divider formed by dc-bias trace parasitic resistance and static electrode-disk overlap capacitors, where (b) very low trace resistance creates a sink for parasitic feedthrough current i_f and increases filter rejection as desired. In contrast, (c) high trace resistance cannot effectively shunt electrical feedthrough, allowing it to leak to the output.

feedthrough, but also minimizes parasitic Q loading of constituent resonators by resistive traces, thereby reducing insertion loss. Low interconnect resistance becomes especially important as electrode-to-resonator gaps shrink to yield correspondingly small resonator motional resistances that are more easily loaded by the interconnect resistance. Disks operating in radial contour modes further derive more benefit than wine-glass counterparts from reduced parasitic trace resistances, since the resonant motional currents for the former enter or leave both input and output electrodes in phase [7]. This makes them more susceptible to resistive loading from dc-bias lines, as well as from input/output lines, both of which degrade the resonator Q , with detrimental impact to filter insertion loss.

As mentioned, raising the structure resistance also reduces parasitic current feeding through the structure. In fact, making the coupling beams non-conductive, as done in [8], would greatly suppress parasitic feedthrough. The benefits of doing this, however, need to outweigh its added process complexity.

B. Case: Balanced Differential Filter

Interestingly, the parasitic feedthrough that plagues the single-ended filter example of the previous sub-section attenuates dramatically when the filter takes on a balanced topology with

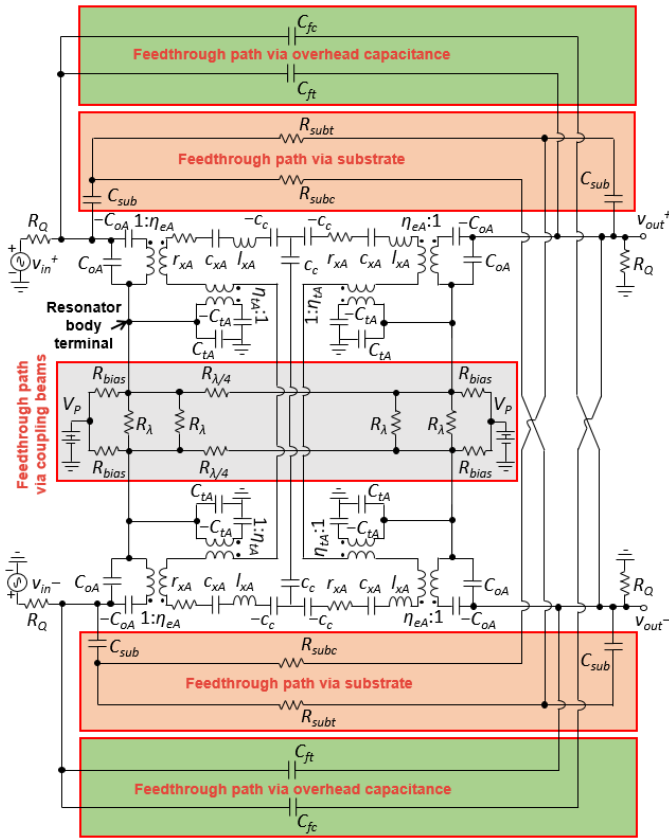


Fig. 9: Electrical equivalent circuit for a 2nd order differential micromechanical disk filter. This circuit improves upon the version presented in Part I of this paper by introducing parasitic electrical feedthrough models as marked in the highlighted rectangular areas. Here, the three dominant feedthrough paths comprise feedthrough via coupling beams, via the substrate parasitic capacitances, and via overhead capacitance.

differential input/output, as in Fig. 1. Here, balanced differential operation generates largely offsetting feedthrough currents at each output node that result in orders of magnitude reduction in feedthrough versus the single-ended case.

The degree of improvement is very clear upon simulation of the equivalent circuit for the entire filter. To this end, Fig. 9 modifies the equivalent circuit of Fig. 24 from part I to explicitly include the most problematic parasitic paths, shown boxed in the figure. Here, resistors $R_{\lambda/4}$ model the resistance across each of the quarter-wavelength coupling beams connecting left and right disk array-composites in the top and bottom halves of the hierarchical structure. Meanwhile, resistors R_{λ} model resistive paths across the full-wavelength beams coupling top and bottom array-composites. Finally, resistors R_{bias} model the equivalent interconnect resistance from the stems to the bias bond pads of the combined resonators in each of the four half-wavelength-coupled array-composites.

Due to their complex structure, parasitic contributions from the disk array-composites are distributed in nature, so are most correctly modeled via circuit networks that mimic the interconnection of all resistors and capacitors in their structures. Doing so reveals that use of a $3\mu\text{m}$ -thick doped polysilicon structure together with $3\mu\text{m}$ -thick doped polysilicon interconnect, such as demonstrated here, yields total parasitic resistance contributions from each array-composite that are negligible compared

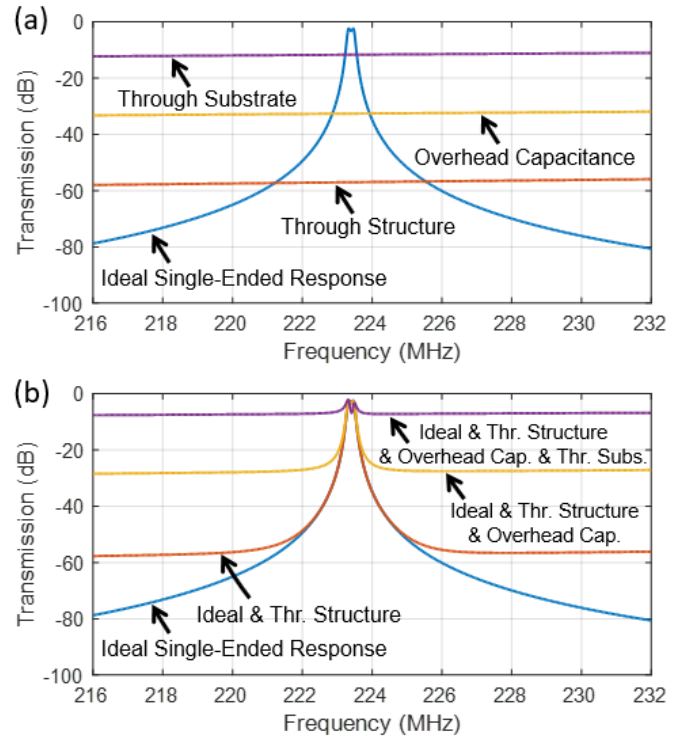


Fig. 10: Single-ended filter response alongside the various feedthrough components. (a) compares the ideal single-ended filter response with individual parasitic feedthrough components, while (b) plots full filter responses as a function of the different feedthrough mechanisms.

with the resistance of the $\lambda/4$ and λ beams that couple them. To unclutter the visual circuit, the model of Fig. 9 ignores the distributed parasitic resistance of the disk array-composites and condenses their equivalent circuits to that used for single resonators, but with element values augmented by the number of resonators used per the theory of Part I.

The efficacy by which balanced differential operation suppresses feedthrough is perhaps best gauged by comparison with the single-ended case. To this end, Fig. 10 uses the top half of the Fig. 9 circuit to simulate the resulting single-ended filter response alongside the various feedthrough components described in the last sub-section. Fig. 10(a) specifically compares the ideal single-ended filter response with individual parasitic feedthrough components, while (b) plots full filter responses as a function of the different feedthrough mechanisms. The plot in (b) for the case where all feedthrough paths are present post a rather meager stopband rejection of only -7.5dB .

For comparison, Fig. 11 presents similar simulations, but for the entire balanced differential filter circuit of Fig. 9, applying a differential input and taking a differential output. The difference is night and day, where cancellation of parasitic feedthrough now permits a stopband rejection of -52.2dB , which is 44.7dB better than the single-ended case.

Clearly, the degree to which the Fig. 9 filter structure is truly symmetric dictates the achievable stopband rejection. Ultimately, despite layout symmetry, practical fabrication mismatch limits the degree of symmetry attainable. With stopband rejection as the gauge, Section VIII will show that the fabrication process herein, together with voltage-controlled frequency tuning, allows for excellent symmetry.

It is worth noting that use of a balanced differential filter at

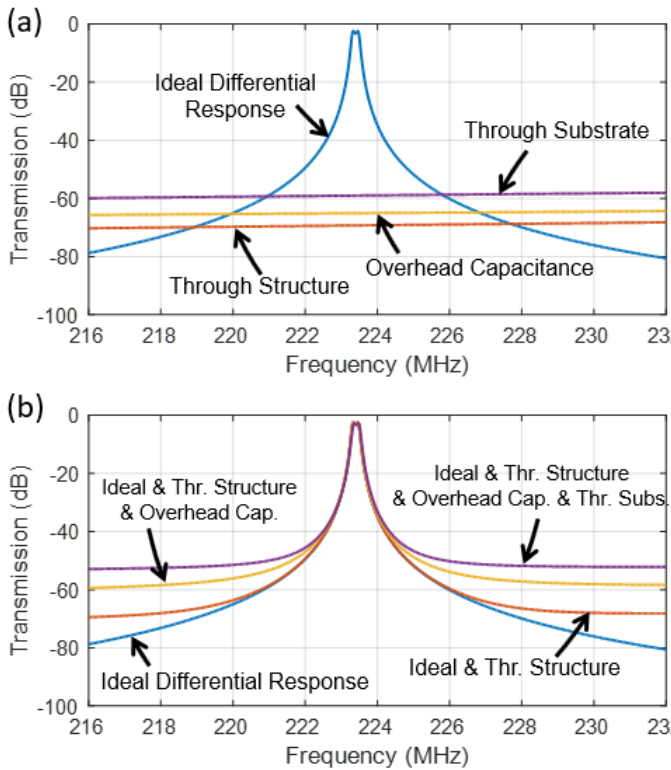


Fig. 11: Differential filter response alongside the various feedthrough components. (a) compares the ideal differential filter response with individual parasitic feedthrough components, while (b) plots full filter responses as a function of the different feedthrough mechanisms, showing superior performance relative to the single-ended case of Fig. 10(b).

an RF front-end might incur some changes from conventional hookups. For example, a balun might now be necessary to go from a single-ended antenna to the input of this balanced differential filter. In addition, an LNA following the filter would need to have a differential input. As a whole, however, balanced differential operation beyond the filter will benefit an RF front-end, e.g., from both noise and linearity perspectives.

V. ELECTRICAL STIFFNESS TUNING OF FREQUENCY MISMATCHES

Small percent bandwidth filters present challenges in not only insertion loss, but also yield and repeatability. Indeed, the smaller the percent bandwidth, the smaller the allowable mismatch between resonators. For example, as illustrated by the simulations of Fig. 12, 0.1% bandwidth requires resonator-to-resonator frequency matching better than 50ppm to limit mismatch-derived pass-band ripple to less than 0.5dB over the designed 0.5dB. So far, single disk resonators (such as used in the arrays of this work) post frequency standard deviations on the order of $\sigma_{f,Single} = 316\text{ppm}$ [9], which is clearly short of the requirement. For this reason, only a small number of the mechanical filters fabricated in [2] actually exhibited acceptable pass-band distortion. Yields of course must be much higher for high volume production.

Reference [9] showed that mechanically-coupled array-composites of resonators attain better matching than any one of their constituents by a factor equal to $\sqrt{N_{tot}}$, where N_{tot} is the total

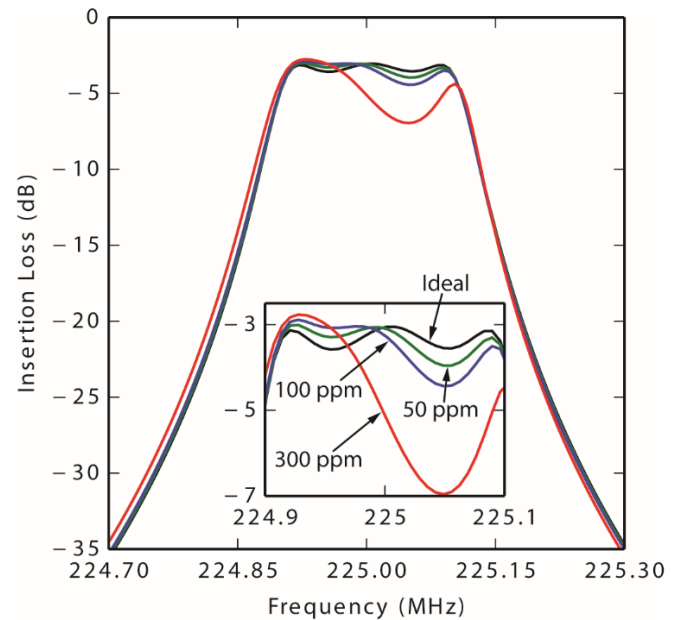


Fig. 12: Simulated frequency response spectra for a 225-MHz three-pole, i.e. three-resonator, 0.5dB-ripple, Chebyshev filter with 0.1% bandwidth, for different amounts of resonator-to-resonator mismatching. For each mismatch case, adjacent resonators experience the indicated frequency deviation in opposite directions to simulate the worst-case mismatch scenario.

number of resonators in the array. Thus, the 48 resonators (including non-I/O ones) used in each differential array-composite pair of Fig. 1 should improve the 316ppm standard deviation by $6.9\times$ to 45.7ppm. This means that about 73% of fabricated filters using the design of Fig. 1 should exhibit acceptable pass-band distortion (defined here as $< 0.5\text{dB}$), with no need for tuning. However, for the more desirable 95% yield, the standard deviation would need to be about 25ppm.

Ultimately, achieving 95% of 0.1% channel-select filters with less than 0.5dB passband distortion requires tuning. The filter of Fig. 1 achieves this by dedicating some of the resonators in each of its mechanically-coupled arrays exclusively for frequency tuning via voltage-controlled electrical stiffness [10]. In this approach, application of a voltage across an electrode-to-resonator gap generates an electric field that varies as gap spacing changes, i.e., as the resonator displaces, in turn, causing the electric force between electrode and resonator to vary in-phase with the change in gap spacing. Any force proportional to and in phase with displacement is, of course, a stiffness, in this case taking the form

$$k_{ej} = \frac{\eta_{ej}^2}{C_{oj}} = \frac{V_{pj}^2 \left(\frac{\partial C}{\partial x}\right)_j^2}{C_{oj}} = \frac{\epsilon_0 A_{oj} V_{pj}^2}{d_{oj}^3} \quad (5)$$

where k_{ej} is the electrical stiffness generated at port j , and η_{ej} , C_{oj} , A_{oj} , $V_{pj} = V_P - V_j$, and d_{oj} are the electromechanical coupling factor, overlap capacitance, overlap area, voltage drop, and spacing, respectively, across the electrode-to-resonator gap of that port.

Although in the demonstrated design of Fig. 1 only 4 resonators out of the 48 in each differential array-composite possess tuning electrodes, any resonator with a voltage across its electrode-to-resonator gap contributes to the total effective electrical stiffness. This includes the 28 I/O resonators in each differential array-composite. Taking this into consideration, the total

frequency-pulling strength of the electrical stiffness imposed on the i^{th} differential array-composite of Fig. 1 using identical disks and electrodes takes the form

$$\omega_{oi} = \sqrt{\frac{N_{tot}k_m - k_{e1} - k_{e2} - \dots - k_{ej}}{N_{tot}m_m}} = \omega_{oim} \sqrt{1 - \frac{\sum_{j=0}^{N_e} k_{ej}}{N_{tot}k_m}} \quad (6)$$

where ω_{oi} is the radian resonance frequency of the i^{th} differential array-composite including electrical effects; N_{tot} is the total number of disk resonators in the differential array-composite; N_e is the total number of electrode-equipped resonators; k_m and m_m are the purely mechanical stiffness and mass, respectively, of each single disk in the array, and ω_{oim} is the purely mechanical radian resonance frequency, i.e., with no voltages applied, given by

$$\omega_{oim} = \sqrt{\frac{N_{tot}k_m}{N_{tot}m_m}} = \sqrt{\frac{k_m}{m_m}} \quad (7)$$

Again, only a subset of the electrodes serve as frequency tuners; the rest connect to the input/output ports. Assuming an applied voltage scheme as in Fig. 1, where the movable structure holds a voltage V_p , all I/O electrodes are at dc ground, and all tuning electrodes at V_t , and further assuming that all disks and electrodes are identical (so dropping the j subscripts), whether they be I/O or tuning, (6) becomes

$$\begin{aligned} \omega_{oi} &= \omega_{oim} \sqrt{1 - \frac{N_{io}V_p^2 \left(\frac{\partial C}{\partial x}\right)^2}{N_{tot}k_m C_o} - \frac{N_t(V_p - V_t)^2 \left(\frac{\partial C}{\partial x}\right)^2}{N_{tot}k_m C_o}} \\ &= \omega_{oim} \sqrt{1 - \frac{N_e}{N_{tot}} \frac{\epsilon_o A_o}{d_o^3 k_m} V_p^2 - \frac{N_t}{N_{tot}} \frac{\epsilon_o A_o}{d_o^3 k_m} V_t(V_t - 2V_p)} \end{aligned} \quad (8)$$

where N_{io} is the number of I/O electrodes, and N_t is the number of tuning electrodes. To better isolate the influence of the tuning voltage V_t , it is often useful to define a nominal resonance frequency equal to the frequency of a differential array without the influence of tuning electrodes. For the case of the Fig. 1 scheme, where without V_t 's all electrode-to-resonator gaps sustain V_p , the nominal resonance frequency of array-composite i is

$$\omega_{oinom} \approx \omega_{oim} \left(1 - \frac{N_e}{N_{tot}} \frac{\epsilon_o A_o}{2d_o^3 k_m} V_p^2\right) \quad (9)$$

which holds when the electrical stiffness due to V_p is much smaller than the pure mechanical stiffness of the array $N_{tot}k_m$. The tuned resonance frequency then takes the form

$$\omega_{oi} \approx \omega_{oinom} \left\{1 - \frac{N_t}{N_{tot}} \frac{\epsilon_o A_o}{2d_o^3 k_m} V_t(V_t - 2V_p)\right\} \quad (10)$$

which again holds when the amount of frequency tuning is very small, e.g., less than 1%, which will be the case, here. From (10), , provided $V_t > 0$, a positive $V_t - 2V_p$ reduces the array-composite frequency from ω_{oinom} , while a negative one raises its frequency. In other words, the bias and tuning scheme of Fig. 1 provides both upward and downward tuning.

In addition to standard deviation advantages already mentioned, the use of disk array-composites provides a flexibility in electrode usage not available with single resonators. In particular, the ability to dedicate some disks for tuning and others for I/O effectively allows frequency tuning without simultaneously affecting I/O transducer efficiency, i.e., without affecting device impedance. This decoupling of tuning and I/O impedance is an important advantage that allows translation of a bandpass

filter's center frequency while maintaining a constant bandwidth—something not easily achievable by the majority of tunable LC and piezoelectric resonator filters that employ varactors for tuning [11] [12].

The main drawback to separation of tuning and I/O resonators is the compromise in transducer strength. Specifically, the impact of converting an I/O resonator to a tuning one is not just the loss of an I/O electrode, but also the addition of the stiffness of a non-I/O resonator to the total array-composite stiffness, which then further degrades the electromechanical coupling (C_x/C_o). When also factoring in the need for stress buffering devices, the $(C_x/C_o)_{prac}$ of a practical array-composite equipped with buffer and tuning reduces from that of an ideal array (where all resonators participate in I/O) by the factor

$$\frac{(C_x/C_o)_{prac}}{(C_x/C_o)_{ideal}} = \frac{N_{io}}{N_{io} + N_b + N_t} \quad (11)$$

where N_b is the number of buffer resonators used. Clearly, to retain maximum electromechanical coupling, one should limit the number of tuning electrodes to as few as needed to overcome the absolute and mismatch frequency tolerances of the prescribed manufacturing process.

To this end, the normalized frequency excursion Δf provided by reasonably sized tuning voltages is important. The expression for this follows readily from algebraic manipulation of (9) and takes the form

$$\Delta f = \frac{\omega_{oinom} - \omega_{oi}}{\omega_{oinom}} \approx \frac{N_t}{N_{tot}} \frac{\epsilon_o A_o}{2d_o^3 k_m} V_t(V_t - 2V_p) \quad (12)$$

To ensure sufficient tuning range to correct for worst-case fabrication mismatch scenarios, a filter designer should choose variables in Table I to satisfy

$$\Delta f \geq \frac{\sigma_{single}}{\sqrt{2N_{tot}}} \quad (13)$$

where σ_{single} is the frequency standard deviation for single constituent resonators in the given manufacturing process, and where the $\sqrt{2N_{tot}}$ term accounts for the reduction in resonance frequency standard deviation when arraying [9].

As illustrated in Fig. 1, each differential array-composite in the filter demonstrated herein dedicates $N_t = 2$ of its $N_{tot} = 24$ resonators for frequency tuning and $N_b = 8$ for stress buffering. Using (12), this resonator utilization scheme with values from Table I yields a frequency pull of 30.2ppm for a 4V change in V_t . This is sufficient to reduce the 45.7ppm frequency standard deviation expected for a 48-resonator array-composite down to the 25ppm needed to constrain mismatch-induced ripple to less than 0.5dB over a designed 0.5dB for 95% of fabricated 0.1% bandwidth filters.

VI. DESIGN PARAMETERS FOR THE FABRICATED 224 MHz, 0.1% BANDWIDTH CHANNEL-SELECT FILTER

Table I and Table II present the result of applying the step-by-step filter design procedure and equations derived in Part I of this paper towards realization of a 224-MHz differential coupled disk resonator filter using the topology of Fig. 1 with a bandwidth $B = 224\text{kHz}$ (i.e., 0.1%) and sub 1-k Ω termination resistors. The resulting mechanical circuit employs 96 resona-

TABLE I: FILTER PHYSICAL DESIGN AND PERFORMANCE SUMMARY

	Parameter	Design Source	Design	Measured	Adjusted / Simulated	Unit
Filter Specifications	Center Frequency, f_o	Spec.	224	223.4	223.4	MHz
	Bandwidth, B	Spec.	224	229	229	kHz
	Percent Bandwidth, P_{BW}	Spec.	0.10	0.10	0.10	%
	Insertion loss, IL	Spec.	2	2.73	2.73	dB
	Minimum Beam Width, $w_{c,min}$	Process	1	1	1	μm
	Out-of-Band Rejection @ $\Delta f = 5\text{MHz}$	Fig. 11	69.6	50.2	49.7	dB
	Filter Termination Resistance, R_Q	(57 [†])	445	590	637	Ω
Filter Design & Material Constants	Normalized q_o	Spec.	10	-	9.0513	-
	Normalized q_n	Spec.	1.9497	-	1.9497	-
	Normalized k_{ij}	Spec.	0.7225	-	0.7225	-
	Young's Modulus, E	Process	158	-	158	GPa
	Density, ρ	Process	2300	-	2300	kg/m^3
	Frequency Material Constant, K_{mat}	(11 [†])	0.654	-	0.654	-
	Disk Mass Adj. Factor, χ	[27 [†]]	0.763	-	0.763	-
Single Disk Resonator	Disk Radius, R	(51 [†])	12.1	12.12	12.127	μm
	Structural Material Thickness, h	Process	3	3	3	μm
	Electrode-to-Resonator Gap, d_o	Process	40	39.1	39.1	nm
	Electrode Span Angle, θ_{ov}	Layout	330	330	330	$^\circ$
	DC bias voltage, V_P	(52 [†])	17	14	14	V
	Resonator Quality Factor, Q	Process	10,000	8,830	8,830	-
	Resonator Electromech. Coupling Coeff., (C_x/C_o)	(17 [†])	0.17	0.13	0.13	%
	Disk Dynamic Mass at Perimeter, m_m	(14 [†])	2.4213	-	2.43	ng
	Disk Dynamic Stiffness at Perimeter, k_m	(14 [†])	4.7963	-	4.79	MN/m
	Disk Damping at Perimeter, b_m	(14 [†])	0.3408	-	0.39	$\mu\text{kg/s}$
Array-Composite Quadrant	Total No. of Disks, N_{tot}	(53 [†] -55 [†])	24	24	24	-
	Rows \times Columns, $N_{row} \times N_{col}$	Layout	4 \times 6	4 \times 6	4 \times 6	-
	Number of Input/Output Resonators, N_{io}	(53 [†])	14	14	14	-
	Number of Buffer Resonators, N_b	Layout	8	8	8	-
	Number of Tuning Resonators, N_t	(55 [†])	2	2	2	-
	Acoustic Quarter-Wavelength, $\lambda/4^{\text{Ⓔ}}$	(59 [†])	9.2503	9.27	9.27	μm
	Filter $5\lambda/4$ Coupling Beam Width, w_c	(60 [†])	5.1664	-	5.3	μm
	Array-Composite $\lambda/2$ and λ Coupling Beam Width	Layout	1	1	1	μm
	Array Electromech. Coupling Coeff., (C_{xA}/C_{oA})	(40 [†])	0.10	0.076	0.076	%

* Boldface value indicates a change from design value needed to curve fit the simulation to actual measured data.

[†] Equation numbers marked with the [†] sign used in this table refer to numbered equations presented in Part I of this paper.

[Ⓔ] The actual quarter wavelength coupler length used is $5\lambda/4$.

TABLE II: FILTER CIRCUIT DESIGN SUMMARY

	Parameter	Source	Design	Measured	Adjusted/ Simulated	Unit	
Core Equivalent Circuit Variables	Inductance at Disk-Composite Array Perimeter, L_{xA}	(62 [†])	58.112	-	58.380	pH	
	Capacitance at Disk-Composite Array Perimeter, C_{xA}	(62 [†])	8.6872	-	8.6863	nF	
	Resistance at disk-composite array perimeter, r_{xA}	(62 [†])	8.1788	-	9.2855	$\mu\Omega$	
	$\lambda/4$ Coupling Beam Lumped Element, c_c	(61 [†])	12.024	-	11.748	μF	
	RF input port static overlap capacitance, C_{oA}	(63 [†])	647.57	-	664.08	fF	
	RF input port coupling coefficient, η_{eA}	(63 [†])	275.22	-	237.78	$\mu\text{C}/\text{m}$	
Tuning Port	Tuning port static overlap capacitance, C_{tA}	(64 [†])	92.510	-	94.869	fF	
	DC tuning voltage, V_t	Measured	17	12.1	12.1	V	
	Tuning port coupling coefficient, η_{tA}	(64 [†])	0	-	4.61	$\mu\text{C}/\text{m}$	
Parasitic Elements	DC bias line resistance, R_{bias}	Measured	0	-	5.85	Ω	
	λ coupling beam resistance, R_λ	Measured	0	-	8	Ω	
	Overhead parasitic capacitances	C_{ft}	Measured	0	-	27.50	fF
		C_{fc}	Measured	0	-	26.86	fF
	Substrate parasitic resistances	R_{subt}	Measured	0	-	378.98	Ω
		R_{subc}	Measured	0	-	388.76	Ω
	Bond pad capacitance, C_{sub}	Measured	0	-	530.5	fF	
	Agilent E5071C I/O Plane Eff. Tuning Inductor, L_{tune}	Measured	0	-	423	nH	

* Boldface value indicates a change from design value needed to curve fit the simulation to actual measured data.

† Equation numbers marked with the † sign used in this table refer to numbered equations presented in Part I of this paper.

tors among 206 resonant elements. The design assumes fabrication via the polysilicon surface-micromachining process flow described in Section VII with a minimum resolvable critical dimension of $w_{c,min} = 1\mu\text{m}$. The design assumes material properties from past experience, specifically $E = 158\text{GPa}$, $\rho = 2300\text{kg}/\text{m}^3$, and $\sigma = 0.226$, for the Young's modulus, density, and Poisson ratio, respectively.

The end result of the design procedure tabulated in Table I comprises not only all relevant geometric dimensions, but also the resulting element values for the electrical equivalent model of Fig. 9 summarized in Table II. In each table, the variables under the column labeled 'Design' indicate the initial design goals assumed during device layout, while values under the column labeled 'Measured' provide the actual measured data obtained either directly from measured plots or curve-fitted to data sets from the fabricated filter structure. The 'Adjusted/Simulated' column provides values used in simulation and shows in boldface parameters introduced or adjusted to match simulated curves using the Fig. 9 circuit to the measured ones. (More on this in Section VIII.)

VII. DISK FILTER FABRICATION PROCESS

Pursuant to verifying the overall design strategy detailed in Part I of this study, the polysilicon vibrating disk filters of this

work were fabricated using a five mask process similar to that of [13] with the cross-sections of major process steps presented in Fig. 13. Given the degrading impact of stress and electrical parasitics outlined in Sections II-IV, the fabrication process employs modifications to the conventional polysilicon surface-micromachining process of [13] to mitigate these effects. In particular, it

- 1) increases the thickness of the doped polysilicon interconnect to reduce interconnect resistance from $21.3\Omega/\square$ at the conventional 300nm-thick to $0.8\Omega/\square$, at the new $3\mu\text{m}$ -thick; and
- 2) employs a generous amount of chemical mechanical polishing (CMP) to eliminate topography during alignment and lithography steps to reduce variance.

The process flow now follows.

A. Fabrication Process Flow Description

The process starts on 6" blank Si wafers with successive LPCVD depositions of $2\mu\text{m}$ LTO and 500nm low-stress silicon nitride at 450°C and 835°C , respectively, to serve as electrical isolation layers; followed by $3\mu\text{m}$ of LPCVD polysilicon deposited at 590°C for 8 hours, then dopes via POCl_3 at 1000°C . Lithography via a first mask and subsequent deep-reactive ion

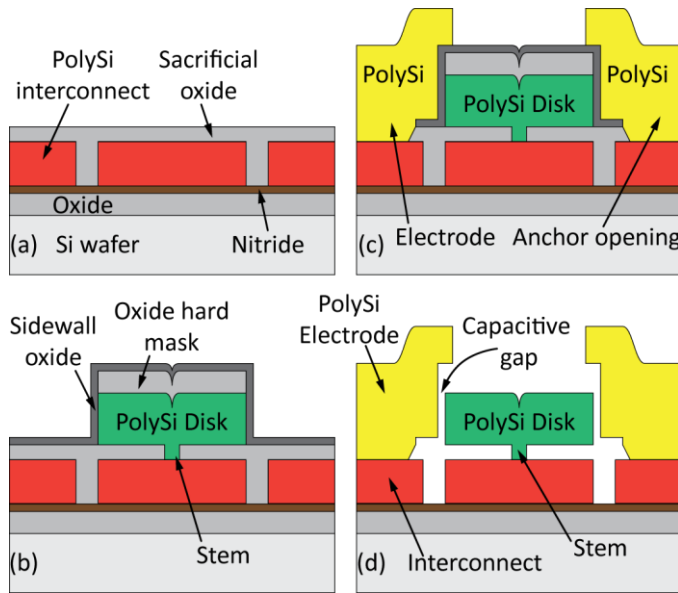


Fig. 13: Cross-sections describing disk filter fabrication process flow after (a) patterning interconnect and depositing bottom sacrificial oxide, (b) depositing structural polysilicon over the stem opening followed by structural layer etch using an oxide hard mask and sidewall sacrificial oxide deposition, (c) opening electrode anchors then filling with doped polysilicon and patterning to form electrodes, and (d) fully released resonator.

etching (DRIE) using an SF_6 chemistry then delineates the interconnect layer, which again due to its much greater thickness than previous processes, offers $0.8\Omega/\square$ sheet resistance. A $3.5\mu\text{m}$ -thick HTO layer is then blanket deposited via LPCVD at 920°C to not only cover the polysilicon, but also to uniformly fill spaces between polysilicon interconnect traces. The CMP step that follows grinds away oxide until it selectively stops on the polysilicon traces, leaving a flat surface composed of oxide and polysilicon interconnect regions. This CMP step eliminates the high topography created by the $3\mu\text{m}$ -thick interconnect routing, and in doing so, facilitates subsequent lithography and etch steps, as well as prevents ripples in the structural resonator film to follow. Next, a blanket 500nm -thick LTO film deposited via LPCVD at 450°C serves as a bottom sacrificial oxide layer (underlying eventual disks) with a uniform thickness over the flattened wafer surface, as depicted in Fig. 13(a). Circular stem openings with $2\mu\text{m}$ diameter are then lithographically defined and etched into the oxide film with the polysilicon interconnect serving as the etch stop.

LPCVD deposition of $3\mu\text{m}$ -thick structural polysilicon at 590°C (followed by POCl_3 doping at 1000°C) then covers the wafer and refills the stem openings etched in the previous step to form the anchor posts of the disk resonators. These mechanical anchors support the disk resonators at their very centers, which correspond to the contour mode vibration nodal points, while also connecting the electrically conductive disk structures to the underlying interconnect layer. A following LPCVD deposition at 450°C of $1.2\mu\text{m}$ -thick oxide then establishes a hard mask layer to be used when etching the thick structural polysilicon. Following a lithography step to delineate the disk structures and coupling beams that form the mechanical filter, RIE using an $\text{Ar}:\text{CHF}_3:\text{CF}_4$ chemistry transfers the filter structure pattern into the oxide hard mask. Any photoresist remaining above the oxide is then removed to avoid polymer formation and photoresist re-deposition on the etch sidewall during the

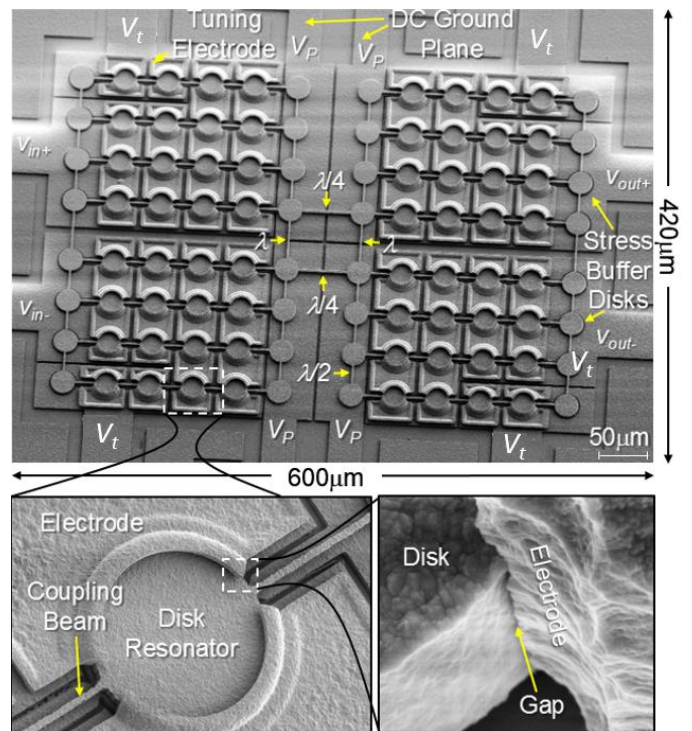


Fig. 14: SEM image of a fabricated and released 2nd order differential filter described schematically in Fig. 1. The left inset zooms in on one of the constituent disk resonator building blocks. The right inset focuses on the tiny (39 nm) capacitive actuation gap between the disk resonator and its electrode.

following structural polysilicon etch step.

The next step—etching the structural material—is vital to many aspects of device performance, from its resonance frequency to its Q to its repeatability. Indeed, etch undercut and smoothness both impact the resonance frequency and its repeatability. The smoothness and straightness of etched structural sidewalls further determine whether or not the desired mode shape ensues, which if not, degrades the achievable Q , especially if the resulting mode shape exhibits vertical motion that pumps energy through the anchor to the substrate. To ensure adequate smoothness and a sidewall angle as close to 90° as possible, exhaustive etch recipe characterization yielded an optimal Lam TCP 9400SE polysilicon RIE etch recipe using gas flow rates of 140sccm of HBr , 14sccm of Cl_2 , and 5sccm of O_2 at 12mTorr pressure with 250W and 75W RF and wafer bias powers, respectively. This recipe etches polysilicon at a rate of $220\text{nm}/\text{min}$ with a polysilicon to oxide etch selectivity of 16:1 and reduces the sidewall roughness compared with higher Cl_2 flow rate recipes. The high selectivity between the oxide hard mask and the structural polysilicon film further enables the desired vertical sidewalls and transfers the layout lateral dimensions to the structural polysilicon film with reduced uncertainty. The efficacy of this recipe derives in part from the tendency of an HBr/Cl_2 based etch chemistry to form sidewall polymer residues containing halogens and silicon oxide [14] that protect sidewalls during etching. This barrier, however, should not be present during subsequent high temperature deposition steps. Removal of sidewall polymer residue entails immersion of wafers into a 50:1 hydrofluoric acid bath for 30 seconds, followed by rinsing in DI water, and finally immersion for 10 minutes in DuPont EKC-270 post-etch residue remover heated to 70°C .

After structural polysilicon patterning comes arguably the

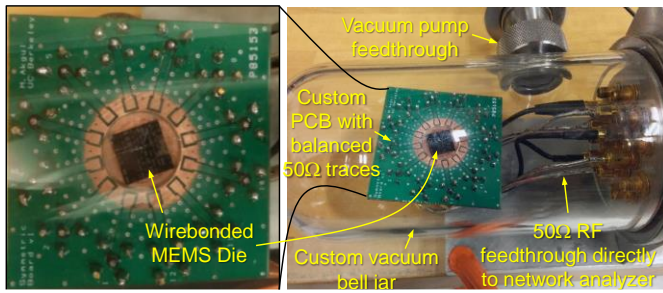


Fig. 15: Vacuum measurement setup using 50Ω RF feedthroughs with matching electrical lengths that connect the network analyzer directly to the wire-bonded micromechanical filter for balanced differential measurement.

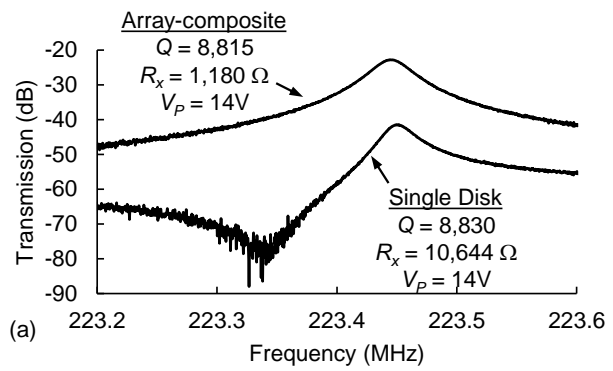
most critical step of the fabrication process: Deposition of the sidewall sacrificial oxide layer that defines the 39nm capacitive actuation gap between the disk and the surrounding electrodes. Here, LPCVD deposition of high temperature oxide (HTO) using 40sccm of DCS and 100sccm of N₂O flow with 600mTorr process pressure at 920°C coats a uniform, conformal, and pin-hole free layer of HTO over the vertical disk sidewalls, as illustrated in Fig. 13(b). Electrode anchor openings are then etched into the bottom oxide sacrificial layer, followed by a blanket LPCVD deposition of 3μm-thick polysilicon and subsequent POCl₃ doping at 1000°C. The final lithography and dry etch steps then define the electrodes, as shown in Fig. 13(c).

Completed wafers are diced and the resulting dies released (when needed) in 49 wt. % liquid HF that frees the filter structure with the final resonator cross-section presented in Fig. 13(d). Fig. 14 presents the SEM image of a fabricated and released 2nd order differential filter that physically realizes the mechanical circuit schematically illustrated in Fig. 1. The insets in Fig. 14 focus in on a constituent disk resonator and coupling beams linking it to other devices in the filter network; and on the tiny capacitive actuation gap formed between the disk resonator and the electrode.

VIII. MEASUREMENT RESULTS

Immediately after fabrication, filters without buffer disks were shorted to their electrodes, and thus, non-functional. The fact that only filters with buffer disks worked, whether single-ended or differential, confirms the importance and efficacy of the buffer-based stress-relief strategy of Section II.

Fabricated differential filters were tested via a four-port direct measurement setup mimicking the circuit of Fig. 1 using an Agilent E5071C network analyzer with the measurement plane moved to the I/O bond pads using standard SOLT calibration, i.e., the instrument compensates out parasitic elements up to the pads. (Since I/O shunt capacitance dominates among parasitics, this essentially amounts to applying an E5071C-simulated tuning inductance.) All measurements used 0dBm, i.e. 0.225V_{rms} signal amplitude, source power settings on all four ports of the network analyzer. During testing, the released MEMS die resides on a board emplaced into in a custom-made vacuum bell jar that provides a 30μTorr vacuum environment as well as ports to allow wired connection to outside measurement instrumentation. Inside the bell jar, wire bonds connect the MEMS die to balanced 50Ω pc-board traces that lead to 50Ω coaxial cable fixtures. These fixtures then permit direct coaxial cable



(a) Comparison of two-port measured frequency spectra for a single disk resonator and a 30-resonator array-composite, with SEM images in (b) and (c).

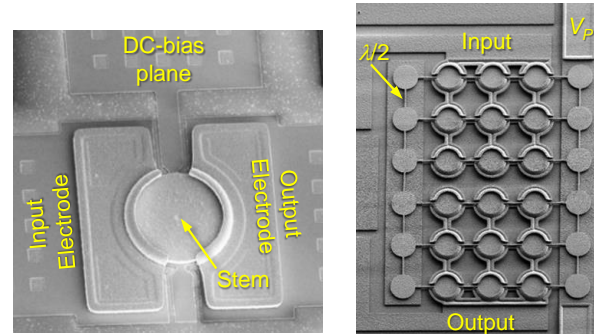


Fig. 16: (a) Comparison of two-port measured frequency spectra for a single disk resonator and a 30-resonator array-composite, with SEM images in (b) and (c).

connection to the network analyzer's 50Ω inputs, as shown in Fig. 15.

Again, the mechanical filter requires a 590Ω termination, so the 50Ω measurement system impedance must be transformed to 590Ω for correct filter operation. Here, the network analyzer's fixture simulator functionality comes in handy, where the network analyzer simulates 590Ω ports from signals measured at its 50Ω ports without the need for any external processing.

In addition to source power applied differentially to the I/O ports with instrument-simulated 590Ω source impedances, Fig. 1 indicates other electrical inputs to the device under test. These include a dc-bias voltage of $V_p = 14V$ applied to the conductive filter structure through the underlying dc-ground plane; as well as DC voltages applied to the indicated frequency tuning pads that connect to non-I/O electrodes purposed for voltage-controlled electrical stiffness tuning, such as described in Section V.

A. Verification of $\lambda/2$ Coupled Array-Composite Operation

To demonstrate the benefits accrued by elevating the design hierarchy from single disk resonators to $\lambda/2$ coupled array-composites, Fig. 16(a) compares the measured two-port frequency spectrum obtained from a single disk resonator shown in (b) with that of a 30-resonator array-composite device shown in (c). Here, both the single disk resonator and those used in the 5×6 array have radii of 12.1μm, which sets their center frequencies at 223.4MHz. As shown, the array composite retains the high $Q > 8,000$ of the single disk resonator while reducing its motional resistance by 9× from 10,644Ω to 1,180Ω for the same

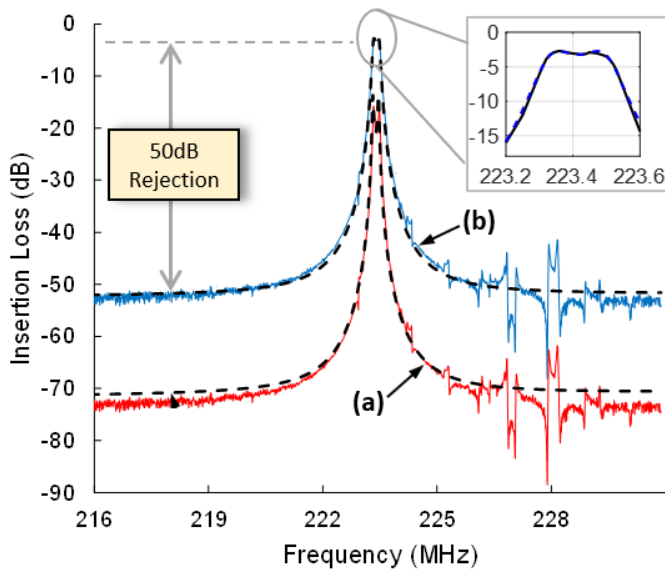


Fig. 17: Comparison of (a) unterminated (i.e. with 50Ω termination) and (b) 590Ω -terminated measured filter spectra (solid lines) together with electrical equivalent circuit simulation results for both cases shown as dashed lines.

bias voltage of $V_p = 14\text{V}$. Note that these are two-port measurements where the dc-bias goes to the suspended structure while one electrode receives the input signal and the other the output signal [15]. The array in this case has the capacitive transduction area of 9 devices, which is smaller than the 14 for each array-composite quadrant of the Fig. 14 filter, so its motional resistance is significantly higher.

Nevertheless, the measured improvement in R_x agrees well with the theoretical expectation derived in Part I of this paper that the improvement factor should be proportional to N_{tot}/N_{io}^2 . Here, $N_{tot} = 30$ is the total number of disks used in the array-composite, including stress-buffer devices in the array perimeter; and $N_{io} = 18$ is the number of resonators with surrounding input/output electrodes. These numbers predict a $10.8\times R_x$ reduction. The slight difference between the measured $9\times R_x$ improvement and the theoretical expectation likely derives from phase mismatches between arrayed resonators that prevent the total summed motional current from attaining the ideal value that would otherwise be delivered to the output node if all resonators vibrated in perfect phase [16]. In addition, although the half- and full-wavelength coupling used should ideally be strong, finite fabrication tolerances can weaken their coupling strengths, so R_x reduction due to vibration localization [17] could still be in play.

Phase deviations or vibration localization notwithstanding, the presented disk array-composite mechanical circuit serves as a good example of enhanced functionality via a building block approach, where the array-composite displays strong agreement between the measurement results and the predicted reduction in R_x while maintaining the high Q and single vibration frequency of a single disk device.

B. Terminated & Electrically Tuned Filter Spectrum

Fig. 17(a) presents the measured filter spectrum as driven and sensed directly by the 50Ω ports of the network analyzer without using its impedance simulation capability. Without the de-

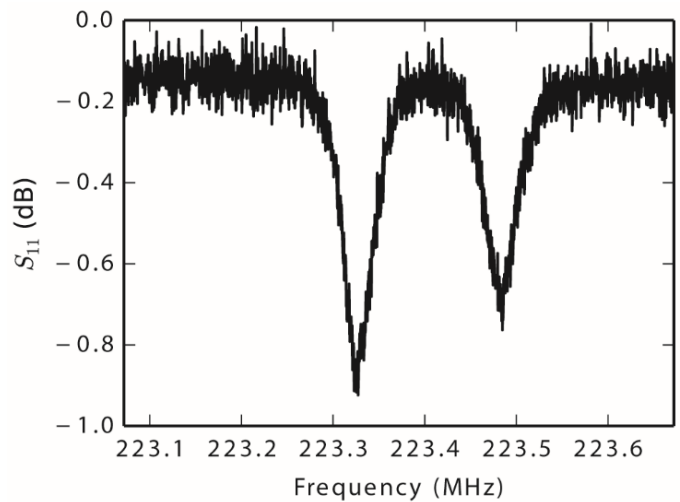


Fig. 18: Measured return loss, i.e. S_{11} , data from the positive-input electrode of the differential filter under identical measurement conditions to those of Fig. 17 with 50Ω termination.

signed 590Ω termination, the measured spectrum is not one expected for a properly designed filter, but rather one with the jagged passband and small stopband rejection shown. As with any filter, whether its resonators are $LCRs$, waveguides, or mechanical resonators, the response does not take on the designed response unless terminated by the designed impedances.

Fig. 17(b) presents the measured, tuned, and terminated filter spectrum with an inset zoom-in on the passband showing it centered at 223.4 MHz with 229-kHz , i.e., 0.1% , bandwidth and only 2.7 dB insertion loss. Here, 590Ω network analyzer-simulated impedances terminate the filter as schematically described in Fig. 1, with a dc-bias voltage of 14V applied to the resonator body and 12.1V to tuning electrodes to correct the filter passband. Small gaps combined with the symmetric and differential design lead to 50 dB out-of-channel rejection and a 20-dB shape factor of 2.7 . This amount of rejection is 23 dB better than a previous capacitive gap transduced differential filter design [2] that did not benefit from low parasitic resistance traces. The 39 nm capacitive transducer gaps of this work generate a single-resonator coupling strength of $C_x/C_o = 0.13\%$, which is $6.4\times$ improvement over previous efforts [2]. However, the array-composite value (with buffer and tuning disks included) shrinks to 0.07% , which is just on the edge of the requirement for an undistorted equipripple passband.

The results presented in succeeding figures, i.e., Fig. 17, Fig. 18, Fig. 19, Fig. 20, Fig. 21, Fig. 23, and Fig. 24, are measured with 0 dBm output power setting applied to all four ports of the network analyzer that corresponds to $0.225\text{ V}_{\text{rms}}$ signal amplitude applied to the I/O electrodes of the filter. Since the device under test is not impedance matched to the 50Ω terminals of the network analyzer, a portion of the applied 0 dBm power reflects back to the source as indicated by the return loss, i.e. S_{11} , data presented in Fig. 18 obtained from the positive-input port of the filter with $Z_o = 50\Omega$ termination. Here, the in-band return loss of 0.9 dB indicates that 81% of the 0 dBm , i.e., 1 mW , applied from the network analyzer port reflects back, and the actual power going through the filter network is $190\mu\text{W}$, i.e., -7.2 dBm , which is considerably above the GSM maximum in-band power

specification of -26dBm. As the zoomed-in inset in Fig. 17 indicates, the filter does not suffer any distortion at -7.2dBm drive power due to Duffing non-linearity. Here, array-composite design is key to raising power handling ability so that the passband distortion under strong inputs that plagued a previous capacitive-gap transduced filter implementation [18] does not occur. Since filter linearity and power handling ability continues to improve with increasing array-size [19] [20], this hierarchical design provides enough design flexibility to accommodate wide dynamic range needs.

The dashed curve in Fig. 17(b) is the theoretical SPICE-simulated prediction via the circuit of Fig. 9 using the element values of Table II. To maximize simulation accuracy, the simulations

- 1) Use the negative-capacitance model [7] for each electrical port to accurately capture electrical stiffness effects, which in turn provide precise filter pole locations for arbitrary port termination impedances.
- 2) Capture the dominant feedthrough paths accurately, as elaborated in Section IV.

The match between measurement and simulation is remarkable and confirms the accuracy of the filter theory and design procedure herein.

C. Measured Group Delay

Fig. 19(a) presents the measured phase response of the terminated filter, along with its group delay [21] in (b) obtained by taking the derivative of (a). To avoid undue distortion or intersymbol interference in digital communication systems, an ideal filter would have constant group delay, or linear phase. Any real filter, of course, has non-constant group delay.

To sufficiently suppress the increase in bit-error rate (BER) instigated by group delay-induced distortion, the group delay variation across the usable filter passband should be less than the period of the fastest processed signal. As a rule of thumb, the group delay should be much less than the reciprocal of the filter bandwidth. How much less depends upon the application, but one reasonable rule of thumb is that it be 1/5 the reciprocal bandwidth. With a bandwidth of 229 kHz, this means the variation in group delay for the demonstrated filter should be on the order of 1 μ s.

Fig. 19(b) shows that the demonstrated filter satisfies this 1 μ s criterion over a usable bandwidth of 128 kHz, which Fig. 20 plots on a zoomed scale. The measured phase and group delay response presented as the solid curves in Fig. 19 are in good agreement with the theoretical expectation plotted as dashed lines obtained by the simulation of the Fig. 9 equivalent circuit using the circuit element values listed in Table II.

D. Spurious Modes

Among the most troubling considerations in practical filter design are spurious modes, i.e., peaks of response at frequencies in the stopband. Suppression of spurious modes often requires creative solutions that are not easily designable and that often result in unique geometries, e.g., the polygons of FBAR filter design [22]. Interestingly, the micromechanical filter design herein suffers much less from these issues, as shown in Fig. 21, which presents the terminated spectrum for the Fig. 14 filter

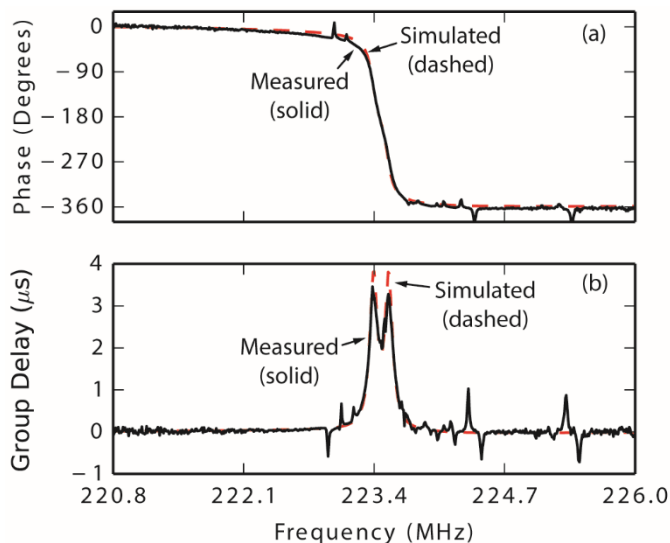


Fig. 19: (a) Phase response, and (b) the corresponding group delay of the differential filter, where the solid curves indicate measured data obtained under measurement conditions identical to Fig. 17, and dashed lines indicate simulated responses obtained from the electrical equivalent circuit of Fig. 9 using the circuit element values listed in Table II.

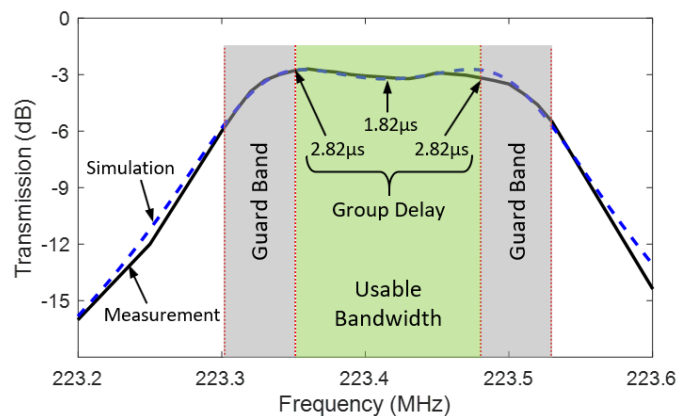


Fig. 20: Terminated filter spectrum indicating usable bandwidth and guard bands that maintain group delay variations below 1 μ s.

over a 100-MHz wide span, showing no strong spurious modes.

The spurious mode advantage evident here arises from two important features of the present filter design: 1) fully balanced differential design, with geometric and electrical symmetry; and 2) the availability of frequency tuning via voltage-controllable electrical stiffnesses. Both of these features used in tandem are instrumental to the Fig. 21 result.

In a similar way that a symmetric and differentially balanced mechanical and electrical design suppresses electrical feedthrough, it also suppresses the spurious vibration mode shapes that might otherwise arise in a complex mechanical network fabricated with finite production precision. As for the case of parasitic electrical feedthrough, if the filter structure is perfectly symmetric, the mechanical mode shape of Fig. 22(a) is undisturbed and only the desired mode ensues. Conversely, any asymmetry introduces mode shape distortion, as finite-element simulated in Fig. 22(b). This distortion effectively generates additional modes, i.e., unwanted spurs.

Perhaps the best testament to the importance of a fully balanced structure for spurious mode suppression comes from

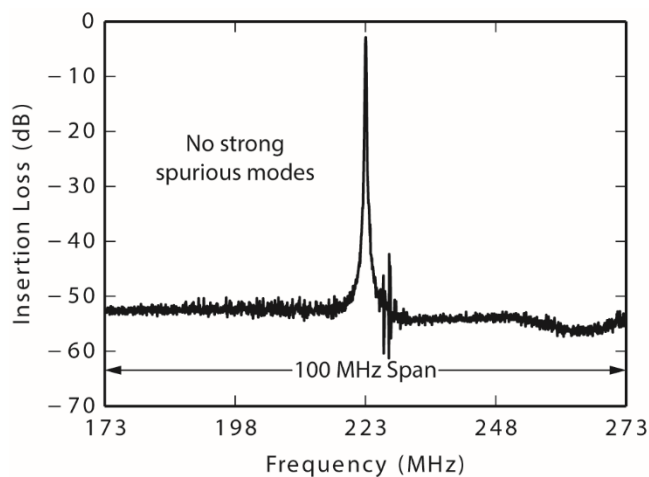


Fig. 21: Measured terminated spectrum over 100 MHz span showing no strong spurious modes.

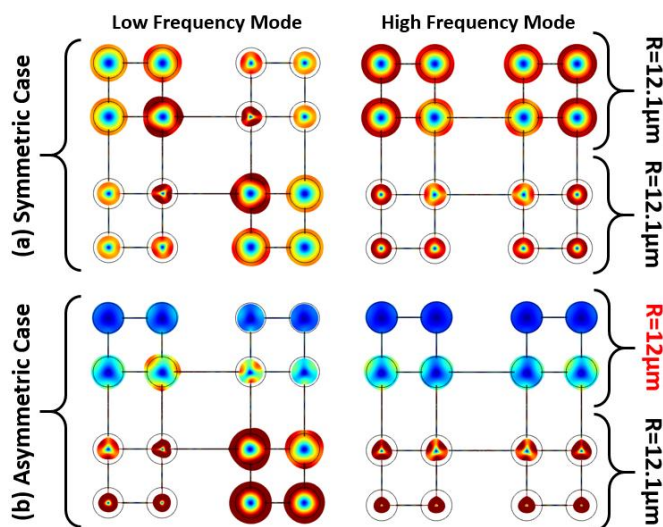


Fig. 22: Mode shapes with (a) full symmetry (b) 1% mismatch between the disk radii at the top and bottom half.

straight comparison of a single-ended design with the fully balanced design of Fig. 14. With this in mind, Fig. 23(b) presents the measured frequency response of the filter structure of Fig. 23(a), which comprises just the top half of the Fig. 14 design, so is not symmetric, not differentially balanced, and takes as input and output single-ended signals. The measured response clearly suffers numerous deficiencies, including feedthrough that reduces the stopband rejection to only 15dB (down from the passband level) and spurious modes only 10dB below the passband level. There is no comparison between this spectrum and that of the symmetric differentially balanced design of Fig. 14.

Clearly, symmetry and balance are key to the much better performance of Fig. 17(b) than Fig. 23(b). Indeed, just the use of a symmetric and fully balanced design affords much better performance than that of a single-ended design. However, improvements in performance to the degree seen in Fig. 17(b) require not only symmetric design, but also the means to perfect the symmetry after fabrication. This is where voltage-controlled

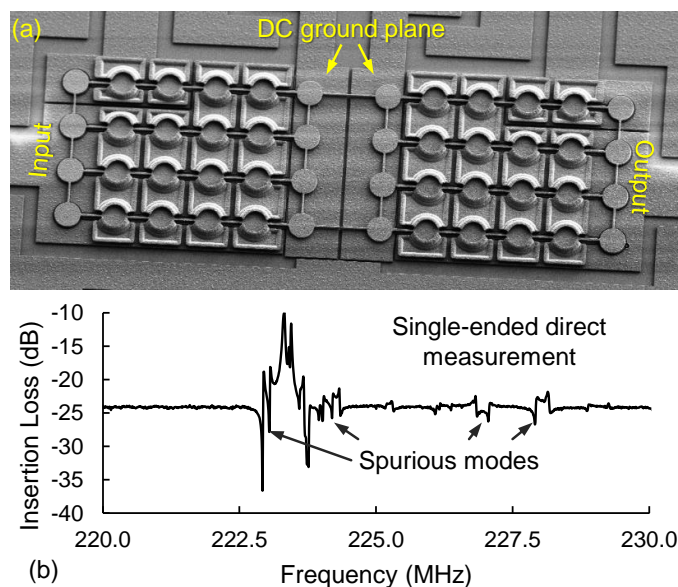


Fig. 23: (a) SEM image and (b) measured 590Ω terminated frequency response of a single-ended version of a disk-array filter, emphasizing the importance of differential design to suppress feedthrough and spurious modes.

frequency tuning provided by electrical stiffness plays an important role.

E. Electrical Stiffness Tuning Strategy

Indeed, post-fabrication voltage-controlled frequency tuning was instrumental to “fixing” not only feedthrough and spurious mode issues, but also the shape of the filter passband response. Fig. 24 emphasizes the importance of electrical tuning for this tiny percent bandwidth filter by demonstrating how proper tuning with 12.1V improves the passband shape and minimizes insertion loss compared to insufficient tuning with 5V and no applied tuning voltage. Here, 2.3dB better insertion loss comes about only after voltage-controlled frequency tuning of the array-composite resonator frequencies.

The optimum tuning voltage was determined empirically by varying V_t and simultaneously monitoring the resulting change in filter frequency response on a network analyzer, until symmetric passband ripple heights were observed around the filter center frequency, which is the expected equiripple passband shape of a Chebyshev filter. The tuning voltage that yields symmetrically positioned passband ripple peaks with equal height also achieves the minimum insertion loss as expected from the closer-to-ideal filter response. This observation is in-line with previous efforts on electrical tuning of kHz frequency capacitive comb-actuated filters [23], [24], where positioning passband resonant peaks equidistant around the filter center frequency via electrical tuning minimized insertion loss and yielded the desired filter response. Automatic tuning techniques using intelligent transistor circuitry would certainly be beneficial in future filter implementations, not only as a low cost post-fabrication tuning method, but also for real-time adaptive compensation of frequency drift over time due to aging or temperature variations.

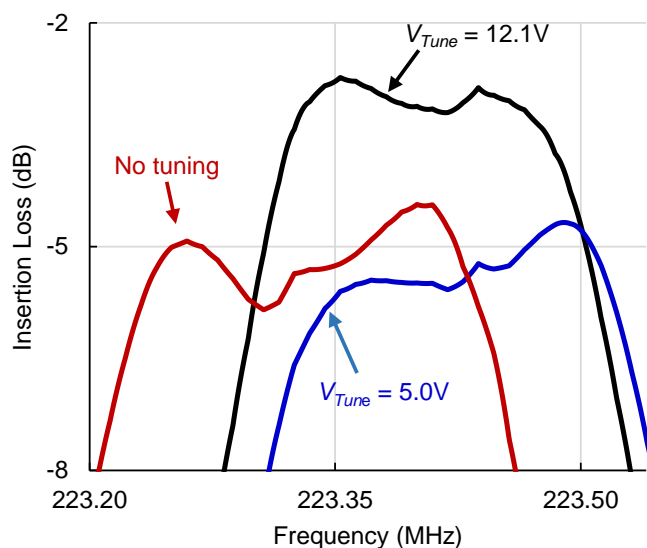


Fig. 24: Measured comparison of terminated filter passband spectrum for varying tuning cases.

IX. CONCLUSIONS

The combined 2.7dB passband insertion loss and 50dB stop-band rejection of the demonstrated 206-element 0.1% bandwidth 223.4-MHz differential micromechanical disk filter represents a landmark for capacitive-gap transduced micromechanical resonator technology. This demonstration proves that the mere introduction of small gaps of around 39nm goes a long way towards moving this technology from a research curiosity to practical performance specs commensurate with the needs of actual RF channel-selecting receiver front-ends. It also emphasizes the need for tuning and defensive stress-relieving structural design when percent bandwidths and gaps shrink, all demonstrated by the work herein.

Perhaps most encouraging is that the models presented in Part I of this study used to design the filter and predict its behavior seem to all be spot on. This means that predictions using these models foretelling GHz filters with sub-200Ω impedances enabled by 20nm-gaps might soon come true, bringing this technology ever closer to someday realizing the ultra-low power channel-selecting communication front-ends targeted for autonomous set-and-forget sensor networks [25] [26] [27]. Work towards these goals continues with renewed encouragement.

X. REFERENCES

- [1] M. Akgul and C. T.-C. Nguyen, "A passband-corrected high rejection channel-select micromechanical disk filter," in *Frequency Control Symposium (FCS), the 2014 IEEE Int.*, May 2014.
- [2] S.-S. Li, Y.-W. Lin, Z. Ren and C. T.-C. Nguyen, "An MSI micromechanical differential disk-array filter," in *Tech. Dig. Int. Conf. Solid-State Sensors, Actuators, and Microsystems (Transducers'07)*, Lyon, France, 2007, pp. 307-311.
- [3] M. Akgul, "A Micromechanical RF Channelizer," in *Ph.D. Dissertation*, Dept. of Electrical Engineering and Computer Sciences, University of California, Berkeley, CA, 2014.
- [4] M. Akgul, B. Kim, Z. Ren and C. T.-C. Nguyen, "Capacitively transduced micromechanical resonators with simultaneous low motional resistance and $Q > 70,000$," in *Tech. Dig. Solid-State Sensors, Actuators, and Microsystems Workshop*, Hilton Head Island, SC, 2010, pp. 467-470.
- [5] J. N. Nilchi, R. Liu and C. T.-C. Nguyen, "High Cx/Co 13nm-capacitive-gap transduced disk resonator," in *Tech. Dig. 30th IEEE Int. Conf. on Micro Electro Mechanical Systems (MEMS)*, Las Vegas, NV, 2017, pp. 924-927.
- [6] C. T.-C. Nguyen, "RF MEMS for channelizing low-power radios," in *Tech. Digest, the 17th Int. Conf. on Solid-State Sensors, Actuators, & Microsystems (Transducers'13)*, Barcelona, Spain, June 16-20, 2013, pp. 2455-2460.
- [7] M. Akgul, L. Wu, Z. Ren and C. T.-C. Nguyen, "A negative-capacitance equivalent circuit model for parallel-plate capacitive-gap-transduced micromechanical resonators," *IEEE Trans. Ultrason., Ferroelect., Freq. Contr.*, vol. 61, no. 5, pp. 849-869, May 2014.
- [8] A.-C. Wong and C. T.-C. Nguyen, "Micromechanical mixer-filters ("mixlers")," *Journal of Microelectromechanical Systems*, vol. 13, no. 1, pp. 100-112, Feb. 2004.
- [9] Y. Lin, W. C. Li, B. Kim, Y.-W. Lin, Z. Ren and C. T.-C. Nguyen, "Enhancement of micromechanical resonator manufacturing precision via mechanically-coupled arraying," in *Proc. Joint IEEE Int. Frequency Control Symp. and European Frequency and Time Forum*, Besançon, France, 2009, pp. 58-63.
- [10] H. Nathanson, W. E. Newell, R. A. Wickstrom and J. R. Davis Jr., "The resonant gate transistor," *IEEE Trans. Electron Devices*, vol. 14, no. 3, pp. 117-133, 1967.
- [11] S. Hao and Q. J. Gu, "A fourth order tunable capacitor coupled microstrip resonator band pass filter," in *Proceedings, 2015 IEEE Radio and Wireless Symp.*, San Diego, California, Jna. 25-28, 2015, pp. 150-152.
- [12] Q. Xiang, Q. Feng, X. Huang and D. Jia, "Electrical tunable microstrip LC bandpass filters with constant bandwidth," *IEEE Trans. Microw. Theory Techn.*, vol. 61, no. 3, pp. 1124-1130, 2013.
- [13] J. Wang, Z. Ren, and C. T.-C. Nguyen, "1.156-GHz self-aligned vibrating micromechanical disk resonators," *IEEE Transactions on Ultrasonic, Ferroelectrics, and Frequency Control*, vol. 51, pp. 1607-1628, Dec. 2004.
- [14] C. C. Cheng, K. V. Guinn, I. P. Herman and V. M. Donnelly, "Competitive halogenation of silicon surfaces in HBr/Cl₂ plasmas studied with x-ray photoelectron spectroscopy and in situ, real-time, pulsed laser-induced thermal desorption," *J. Vacuum Science and Technology A: Vacuum Surfaces and Films*, vol. 13, no. 4, pp. 1970-1976, 1995.
- [15] J. R. Clark, W.-T. Hsu and C. T.-C. Nguyen, "Measurement techniques for capacitively-transduced VHF-to-UHF micromechanical resonators," in *Tech. Dig. Int. Conf. Solid-State Sensors, Actuators, and Microsystems (Transducers'01)*, Munich, Germany, 2001, pp. 1118-1121.
- [16] M. Akgul, Z. Ren and C. T.-C. Nguyen, "Voltage-controlled tuning to optimize MEMS resonator array-composite output power," in *Proc. Joint IEEE Int. Frequency Control Symp. and European Frequency and Time Forum*, San Francisco, CA, 2011, pp. 1-6.
- [17] A. Erbes, P. Thiruvengatanathan, J. Woodhouse and A. A. Seshia, "Numerical study of the impact of vibration localization on the motional resistance of weakly coupled MEMS resonators," *IEEE J. of Microelectromechanical Syst.*, vol. 24, no. 4, pp. 997-1005, Aug. 2015.
- [18] S.-S. Li, M. U. Demirci, Y.-W. Lin, Z. Ren and C. T.-C. Nguyen, "Bridged micromechanical filters," in *Proc. Joint IEEE Int. Frequency Control Symp. and European Frequency and Time Forum*, Montreal, Canada, 2004, pp. 144-150.
- [19] M. U. Demirci and C. T.-C. Nguyen, "Mechanically corner-coupled square microresonator array for reduced series motional resistance," *J. Microelectromech. Syst.*, vol. 15, no. 6, pp. 1419-1436, 2006.
- [20] C.-Y. Chou, M.-H. Li, C.-Y. Chen, C.-Y. Liu and S.-S. Li, "An innovative 3-D mechanically-coupled array design for MEMS resonator and oscillators," in *Tech. Digest, the 19th Int. Conf. on Solid-State Sensors, Actuators, & Microsystems (Transducers'17)*, Kaohsiung, Taiwan, Jun 18-22, 2017, pp. 90-93.

- [21] A. S. Sedra and P. O. Brackett, *Filter Theory and Design: Active and Passive*, Beaverton, OR: Matrix, 1978.
- [22] J. D. Larson, III, R. C. Ruby and P. Bradley, "Bulk acoustic wave resonator with improved lateral mode suppression". U.S. Patent 6 215 475 B1, 10 April 2001.
- [23] K. Wang and C.-C. Nguyen, "High-order medium frequency micromechanical electronic filters," *J. Microelectromech. Syst.*, vol. 8, no. 4, pp. 534-557, 1999.
- [24] H. G. Barrow and C. T.-C. Nguyen, "A protocol for automated passband correction of high-order microelectromechanical filters," in *Proc. IEEE Int. Frequency Control Symp.*, Taipei, Taiwan, 2014, pp. 1-5.
- [25] C. T.-C. Nguyen, "MEMS-based RF channel selection for true software-defined cognitive radio and low-power sensor communications," *IEEE Commun. Mag.*, vol. 51, no. 4, pp. 110-119, 2013.
- [26] J. W. Park and B. Razavi, "Channel selection at RF using Miller bandpass filters," *IEEE J. of Solid-State Circuits*, vol. 49, no. 12, pp. 3063-3078, Dec. 2014.
- [27] J. M. Rabaey, J. Ammer, T. Karalar, S. Li, B. Otis, M. Sheets and T. Tuan, "PicoRadios for Wireless Sensor Networks: The Next Challenge in Ultra-Low Power Design," in *Tech. Dig. Int. Solid-State Circuits Conf.*, San Francisco, CA, 2002, pp. 200-201.



Mehmet Akgul (S'07) received the Ph.D. in Electrical Engineering and Computer Sciences at the University of California at Berkeley in 2014. He received the B.S. degree in Electrical and Electronics Engineering from the Middle East Technical University, Ankara, Turkey, as second in his class in 2007.

His PhD research focused on the design, microfabrication, and testing of medium-scale integrated micromechanical circuits using capacitive-gap transduced resonators as building blocks, with a primary focus on RF filters for ultra-low power radio applications. He also studied diamond materials for high- Q mechanical resonators and explored the use of ALD high- k dielectrics to strengthen electromechanical coupling by partially filling electrode-to-resonator gaps towards the sub-40 nm range.

In 2014, he joined TDK InvenSense as a Sr. MEMS Design Engineer, where he worked as a MEMS inertial measurement unit (IMU) designer with a specific focus on optical image stabilization (OIS) gyroscopes. In 2015, he joined Google, where he is presently a Sr. Hardware Design Engineer. His current focus is on sensor fusion algorithms for better location and context user experience in mobile platforms.



Alper Ozgurluk (S'12) received the B.S. degree in Electrical and Electronics Engineering from Bilkent University, Ankara, Turkey. He is currently working towards his Ph.D. degree in Electrical Engineering and Computer Sciences at the University of California at Berkeley.

His research interests include capac-

itive-gap transduced large-scale integrated (LSI) micromechanical circuits, high- Q wide-tunable ruthenium metal resonators, and integrated CMOS-MEMS systems.



Clark T.-C. Nguyen (S'90-M'95-SM'01-F'07) received the B. S., M. S., and Ph.D. degrees from the University of California at Berkeley in 1989, 1991, and 1994, respectively, all in Electrical Engineering and Computer Sciences.

In 1995, he joined the faculty of the University of Michigan, Ann Arbor, where he was a Professor in the Department of Electrical Engineering and Computer Science up until mid-2006.

In 2006, he joined the Department of Electrical Engineering and Computer Sciences at the University of California at Berkeley, where he is presently the Conexant Systems Distinguished Professor and a Co-Director of the Berkeley Sensor & Actuator Center. His research interests focus upon micro electromechanical systems (MEMS) and include integrated micromechanical signal processors and sensors, merged circuit/micromechanical technologies, optomechanical devices, RF communication architectures, and integrated circuit design and technology. In 2001, Prof. Nguyen founded Discera, Inc., a company aimed at commercializing communication products based upon MEMS technology, with an initial focus on the very vibrating micromechanical resonators pioneered by his research in past years. He served as Vice President and Chief Technology Officer (CTO) of Discera until mid-2002, at which point he joined the Defense Advanced Research Projects Agency (DARPA) on an IPA, where he served for four years as the Program Manager of ten different MEMS-centric programs in the Microsystems Technology Office of DARPA.

Prof. Nguyen won the IEEE Cady Award in 2006, the IEEE Robert Bosch Micro and Nano Electro Mechanical Systems Award in 2017, and together with his students has garnered more than twelve best paper awards from IEEE conferences and journals focused on frequency control and MEMS. From 2007 to 2009, he served as a Distinguished Lecturer for the IEEE Solid-State Circuits Society. Prof. Nguyen was the Technical Program Chair of the 2010 IEEE Int. Frequency Control Symposium and a Co-General Chair of the 2011 Combined IEEE Int. Frequency Control Symposium and European Frequency and Time Forum, as well as a Co-General Chair of the 2017 IEEE Int. Micro Electro Mechanical Systems Conference. From 2008 to 2013, he served as Vice President of Frequency Control in the IEEE Ultrasonics, Ferroelectrics, and Frequency Control Society, after which he became the society President from 2016 to 2017. He is currently the Junior Past-President of the society.